Local structure of potassium doped nickel oxide: A combined experimental-theoretical study

Friederike Wrobel,[1] Hyeondeok Shin,[2] George E. Sterbinsky,[3] Haw-Wen Hsiao,[4] Jian-Min Zuo,[4] P. Ganesh,[5] Jaron T. Krogel,[6] Anouar Benali,[2,7] Paul R. C. Kent,[5,8] Olle Heinonen,[1,9] and Anand Bhattacharya[1]

[1]*Materials Science Division, Argonne National Laboratory, Lemont, Illinois 60439, USA*
[2]*Computational Science Division, Argonne National Laboratory, Argonne, Illinois 60439, USA*
[3]*X-ray Science Division, Argonne National Laboratory, Argonne, Illinois 60439, USA*
[4]*Department of Materials Science and Engineering, University of Illinois at Urbana-Champaign, Urbana, Illinois 61801, USA*
[5]*Center for Nanophase Materials Sciences, Oak Ridge National Laboratory, Oak Ridge, Tennessee 37831, USA*
[6]*Materials Science and Technology Division, Oak Ridge National Laboratory, Oak Ridge, Tennessee 37831, USA*
[7]*Leadership Computing Facility, Argonne National Laboratory, Argonne, Illinois 60439, USA*
[8]*Computational Sciences and Engineering Division, Oak Ridge National Laboratory, Oak Ridge, Tennessee 37831, USA*
[9]*Center for Hierarchical Material Design, Northwestern-Argonne Institute for Science and Engineering, Northwestern University, Evanston, Illinois 60208, USA*

(Received 28 August 2019; published 18 November 2019)

The electronic structure of Mott and charge-transfer insulators can be tuned through charge doping to achieve a variety of fascinating physical properties, e.g., superconductivity, colossal magnetoresistance, and metal-to-insulator transitions. Strong correlations between d electrons give rise to these properties but they are also the reason why they are inherently difficult to model. This holds true especially for the evolution of properties upon charge doping. Here, we hole-dope nickel oxide with potassium and elucidate the resulting structure by using a range of experimental and theoretical tools; potassium is twice as big as nickel and is expected to lead to distortions in its vicinity. Our measurements of the x-ray absorption fine structure (XAFS) show a significant distortion around the dopant and that the dopant is fully incorporated in the nickel oxide matrix. In parallel, the theoretical investigations include developing a Gaussian process for quantum Monte Carlo calculations to determine the lowest energy local structure around the potassium dopant. While the optimal structures determined from density functional theory and quantum Monte Carlo calculations agree very well, we find a large discrepancy between the experimentally determined structures and the theoretical doped structures. Further modeling indicates that the discrepancy is likely due to vacancy defects. Our work shows that potassium doping is a possible avenue to doping NiO, in spite of the size of the potassium dopant. In addition, the Gaussian process opens up a new route towards obtaining structure predictions outside of density functional theory.

DOI: 10.1103/PhysRevMaterials.3.115003

I. INTRODUCTION

Doped transition metal oxides display some of the most fascinating and potentially useful properties. For example, cables made of high-temperature superconducting cuprates [1] have been installed in cities around the globe to improve the efficiency of electrical power transport [2]. The electrical properties of transparent p-type conducting oxides, like NiO, can be tuned through doping, which is useful for applications in solar cells and electronics [3]. NiO doped with potassium is also of interest as a catalyst [4,5], and as a high-permittivity material [6]. Furthermore, memory technologies based on correlated oxides may push the limit of storage density further as conventional semiconductor memory is expected to soon hit its physical limits [7].

However, in order to exploit properties of doped correlated oxides we must first gain a fundamental understanding of how chemical and electronic structures evolve upon doping. NiO is a canonical correlated transition metal oxide with a simple rock salt structure, but also, as mentioned above, interesting from the point of view of applications. This makes NiO an excellent model system, both experimentally and theoretically, for correlated insulating oxides. Standard band theory predicts NiO to be metallic but strong on-site correlations drive it to be insulating. The nickel e_g levels are split into an upper and a lower Hubbard band and a gap opens between the oxygen $2p$ states and the upper Hubbard band, therefore making nickel oxide a charge-transfer insulator [8]. It orders antiferromagnetically [9] below ~520 K with the nickel spins aligned ferromagnetically within the (1,1,1) planes of the rocksalt structure and antiferromagnetically between those planes [10].

NiO can be hole doped; for example, by substitutional doping of Li. Li^+ dopants order in alternating Li-rich and Li-poor rocksalt (1,1,1) planes. At low doping the order is of short range but develops into long-range order above a doping level of about 35%. The magnetic order develops accordingly—antiferromagnetic with reduced Néel temperature at low doping, and ferrimagnetic above ~35% [11]. At a doping level of 50% ($=Li_{0.5}Ni_{0.5}O$), the ordering is close to perfect, layers of Ni^{3+} alternate with layers of Li^+, and (Li,Ni)O adopts a glassy, antiferromagnetic state below 7.5 K [12]. The doped holes created by Li^+ doping have oxygen p character as was shown by oxygen K-edge

x-ray absorption spectroscopy (XAS) [13]. Rather than creating holes in an otherwise unchanged oxygen p band, the holes form impurity states within the band gap, thereby preventing the system from going metallic. The strong exchange coupling between holes in the oxygen $2p$ levels and nickel $3d$ states leads to an observation of apparent low-spin nickel $3d^7$ in macroscopic measurements [13].

Despite decades of experimental studies and efforts to describe the electronic structure theoretically, the interactions between nickel oxide's highly correlated d electrons are not described accurately within today's models [14], which primarily rely on density functional theory (DFT) [15,16].

DFT is in principle exact, but exchange interactions and electronic correlations have to be approximated by exchange-correlation functionals. These functionals have greatly improved over the years and DFT has been successfully used to predict numerous lattice structures and band structures [17]. For strongly correlated systems, the "Hubbard U" or "DFT + U" approach is often used to describe the strong on-site correlations of d and f electrons within density functional theory (DFT). Through including the additional Hubbard U term and through tuning it, a good approximation of the band structure of correlated materials can be obtained, including the band gap. The magnitude of U, however, is determined mostly empirically. In particular a single parameter U is may not be sufficient to describe the whole correlated electron system upon charge doping, since it should vary with local atomic environment.

A relatively young approach to describe these strong correlations is quantum Monte Carlo (QMC) [14,18]. QMC treats the electron-electron interactions explicitly and accurately with few approximations, and therefore has the potential to overcome the shortcomings of DFT while being computationally less expensive than, for example, full configuration interaction and full coupled cluster calculations [19]. The method, however, is still in its infancy and many tools, e.g., structural optimization, which is a staple in all other electronic structure theories, need to be developed.

In the present work, we study the structure of NiO thin films doped with potassium, grown by molecular-beam epitaxy (MBE), using a range of experimental and theoretical tools. In contrast with the small size of Li dopants, the ionic radius of potassium is about twice that of nickel [20]. The large size of potassium as a dopant is expected to lead to distortions around it, and may also lead to problems dispersing K dopants throughout the NiO matrix. The large size also limits the solid solubility of K in NiO. Based on our own calculations (see below as well as Ref. [21]), the strain around a K dopant has barely relaxed by the closest Ni shell. In and of itself, this rapid relaxation of the strain is remarkable. However, it suggests that at K concentrations exceeding about 25% the strain fields will interact, leading to a large increase in elastic energy that would probably lead to phase separation. This is consistent with the results in Ref. [22], in which x-ray diffraction patterns at 25% concentration still showed evidence of good crystallinity, but where trends in conductivity and mobility changed at doping levels of 20% to 25%. We have grown K-doped thin films with doping concentration of up to about 9% without any discernible changes in x-ray diffraction patterns, suggesting high-quality crystalline structures at these doping levels. To accurately predict these distortions, we developed a Gaussian process (GP) for structural optimization using QMC. We compared the results from the GP with the DFT results and with the experimentally determined local structure. We achieved the latter through an analysis of the x-ray absorption fine structure (XAFS) of the potassium K edge as well as strain mapping by using transmission electron microscopy (TEM). Our analyses show that potassium is indeed dispersed throughout the NiO film, demonstrating its use as a chemical dopant. However, we found that the local distortions around the potassium dopant are significantly larger (about 0.35 Å for the K–O bond length) than predicted by theory; both DFT and QMC. Further studies of defect structures using *ab initio* molecular dynamics indicate that the large K–O bond length derives from oxygen vacancies near two potassium dopants, even at low concentration.

II. METHODS

A. Sample preparation and characterization

Stoichiometric and potassium-doped NiO thin films were grown on the atomically flat (100) surfaces of rocksalt-type MgO substrates and perovskite-type $NdScO_3$ substrates. Before growth, the substrates were cleaned with acetone and isopropanol in an ultrasonic bath and annealed for a few minutes at 600 °C in 1×10^{-6} mbar ozone atmosphere. Ni and K were evaporated from effusion cells at a substrate temperature of 200 °C and in a 4×10^{-7} mbar ozone atmosphere.

NiO film thickness and c-axis parameter were measured with low-angle x-ray reflectivity and θ-2θ scans through the (002) reflections of film and substrate, respectively (for details see Supplemental Material [23]). The composition of all samples was measured with Rutherford backscattering (RBS) and analyzed by using the SIMNRA software [24].

B. X-ray absorption fine structure

X-ray absorption fine structure (XAFS) was measured at the bending magnet beamline 9-BM of the Advanced Photon Source, Argonne National Laboratory, by using a Si(111) double crystal monochromator and a four-element silicon drift detector for fluorescence detection. The samples were mounted on a spinning stage with an incidence angle of about 25°. For the measurements at the potassium K edge, the sample was placed in a helium-filled chamber. We tested both polarizations (in-plane and out-of-plane) but observed no significant difference.

We collected data at the Ni K edge for an undoped sample (12 nm NiO grown on MgO, data shown and discussed in the Supplemental Material [23]). MgO substrates contain a small Ca impurity and the Ca K edge is only 430 eV above the potassium K edge, which prevents measurement above $k = 10.5$ Å^{-1}. To measure XAFS at the potassium K edge we used a 42-nm-thick (K, Ni)O film with a doping level of 3.9%, grown on $NdScO_3$ instead of MgO. The lattice mismatch between NiO and $NdScO_3$ is as big as 4%. To avoid the additional complication of the K–O distance changing according to the relaxation in the NiO matrix, we added a buffer layer of 12 nm NiO between the substrate and the K-doped region.

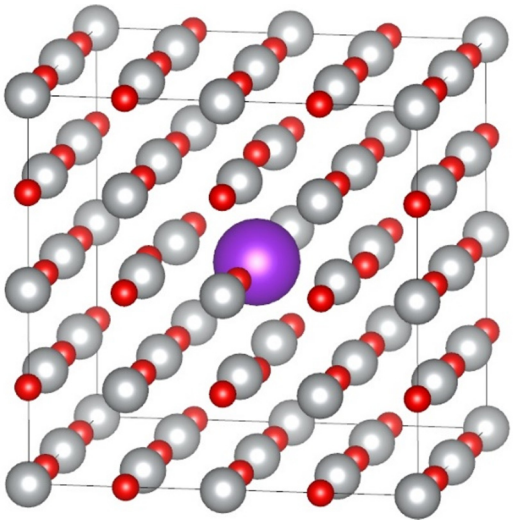

FIG. 1. Crystal structure of $K_{0.03}Ni_{0.97}O$. Purple, gray, and red spheres represent K, Ni, and O atoms, respectively.

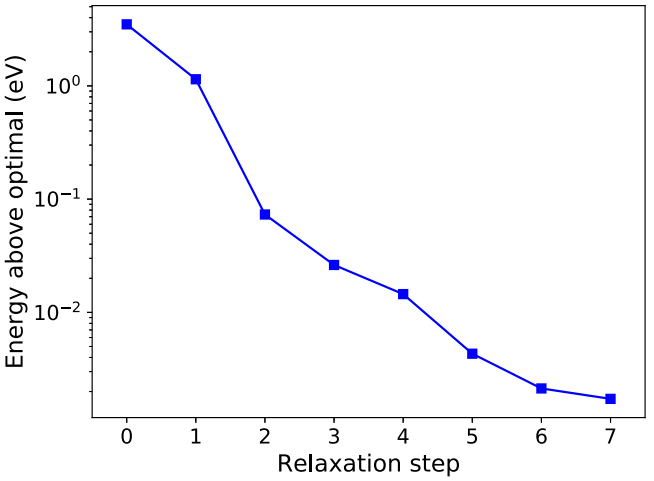

FIG. 2. Energy convergence of K-NiO structure relaxation via DFT (PBE) force optimization. Total energies are shown relative to the final converged energy as a function of relaxation step in the optimization process.

Within the thickness of 12 nm the in-plane lattice parameters of NiO relax fully to its bulk value. Therefore, we can safely assume that the lattice parameters across the thickness of the K-doped region do not change. Finally, to prevent possible surface reactions, we added a 2 nm NiO capping layer.

C. Calculations using density functional theory and quantum Monte Carlo

The atomic structure of K-doped NiO (K-NiO) was obtained theoretically both with DFT-based methods [15,16] and a combination of variational Monte Carlo (VMC) [25] and Gaussian process (GP) regression [26,27]. The K-NiO structure was represented in a 64-atom cubic periodic supercell, with a G-type antiferromagnetic ordering of the moments on the Ni atom. The K–O bond length of the relaxed structures was confirmed to be minimally changed in larger supercell models at the DFT level. DFT relaxation paths were analyzed to extract a low parameter model for the relaxation, appropriate for structural optimization with VMC coupled with Gaussian process regression.

1. **K-NiO** *geometry optimization using density functional theory*

To study the bond lengths in bulk NiO doped substitutionally with K, we optimized the K-doped NiO geometry using DFT with a plane-wave basis set as implemented in the QUANTUM EXPRESSO package [28]. We used the 64-atom NiO supercell with a G-type antiferromagnetic ordering, with K substituting one Ni atom ($K_{0.03}Ni_{0.97}O$) cell (see Fig. 1). A pure NiO 64-atom structure with the experimental Ni–O bond length of 2.08 Å [29] was used as initial geometry and one Ni atom in the NiO was replaced with a K. The K-doped NiO geometry was fully relaxed within the Kohn-Sham scheme until Hellman-Feynman forces acting on the atoms decreased to below 10^{-2} eV/Å. When optimizing the geometry, various DFT exchange-correlation (XC) functionals, LDA [30,31], PBE [32,33], LDA + U [34], and PBE + U, were considered in order to investigate the dependence of the optimized bond lengths on the choice of XC functional. For the PBE + U and LDA + U calculations, we applied a Hubbard U, using the rotationally invariant Dudarev method [35], on the Ni atom d orbitals with a value of 6.8 eV (LDA) and 4.7 eV (PBE), which were obtained through minimizing diffusion Monte Carlo (DMC) [36] energies in a previous study for pure NiO [21]. Scalar-relativistic ultrasoft pseudopotentials were used in the geometry optimization, and $4 \times 4 \times 4$ Monkhorst-Pack grids were used with a 100 Ry kinetic energy cutoff and 800 Ry density cutoff.

2. Reduced structure model of **K-NiO** *for Gaussian process optimization*

As described above, the full K-NiO structure considered contained 64 atoms in a cubic periodic supercell with a G-type antiferromagnetic ordering. The broadest parameter space to search for this structure contains 192 continuum degrees of freedom, which is far too large to be practical with GP. To apply GP regression effectively, a reduced structure model was sought to parametrize important degrees of freedom.

First, a representative relaxation pathway was obtained within density functional theory. The K-NiO structure was force optimized via the PBE functional with no constraints imposed. The initial unrelaxed structure was obtained by replacing a single Ni atom with K in the experimental NiO bulk geometry. The energetic convergence of the PBE optimization procedure is shown in Fig. 2.

Next, the final displacements of the atoms were grouped by magnitude. Absolute atomic displacements that differed by no more than 0.00033 Å were considered to be equivalent. This grouping procedure—which in part reflects point-group symmetry—resulted in ten displacement groups, reducing the total number of free parameters from 192 to 10.

The parametric complexity of the structure model was further reduced by considering displacements that were related approximately linearly along the PBE relaxation path. In Fig. 3, the ten displacement groups are shown along the relaxation pathway normalized relative to final displacement.

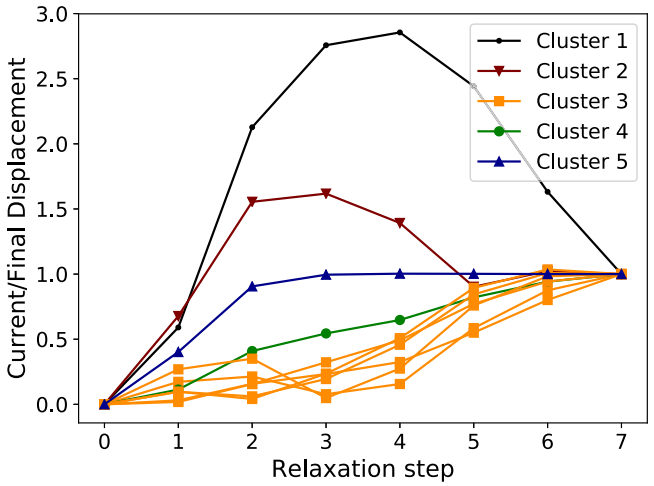

FIG. 3. Current displacements along the PBE relaxation path scaled by final displacement for each of the ten identified displacement groups. Displacement groups showing a near-linear relationship are clustered, which is shown by different colors in the figure. Following this linear clustering, five effective parameters remain.

Displacement groups that moved in concert were combined according to the color-coded clusters shown in Fig. 3. This resulted in six of the original displacement groups being combined into a single group, resulting in a five-parameter model. The six groups combined in this way actually correspond to the six K–O bond lengths in the structure that undergo the largest displacements. One displacement group corresponded to minuscule atomic relaxations (displacements smaller than 7×10^{-5} Å away from the initial unrelaxed structure). These displacements are not significant on the scale of the total relaxation energy and so can be safely excluded. In the subsequent VMC relaxation via GP regression, these displacements were held fixed at zero, resulting in an effective four-parameter structure model.

3. *Gaussian process structural optimization*

Gaussian process [27] regression is a statistical approach to interpolate high-dimensional functions with minimal information. From the point of view of GP, the entire high-dimensional function is viewed as a sample from an infinite-dimensional Gaussian distribution. This distribution is usually assumed to have zero mean, and a model must be explicitly assumed for the covariance. Some of us previously applied GP to a molecular system [26], but we now apply it to a defect in QMC. In this study, we are interested in the lowest-energy structure of K-NiO, and so we are aiming to find the minimum of an as-yet-unknown energy surface $E(p)$ that depends on a vector of parameters, p. The parameters can be direct atomic coordinates or underlying variables that determine atomic coordinates. Given two sets of points P and P' of size N and N' in this parameter space, the $N \times N'$ covariance matrix K between the two sets of points is

$$K(P, P') = \begin{bmatrix} k(p_1, p'_1) & \cdots & k(p_1, p'_{N'}) \\ \vdots & \ddots & \vdots \\ k(p_N, p'_1) & \cdots & k(p_N, p'_{N'}) \end{bmatrix},$$

where $p_i \in P$, $p'_j \in P'$, and $k(p, p')$ is a chosen covariance function. For this study, we have chosen the squared exponential covariance function

$$k(p, p') = \exp\left(-\frac{\|p - p'\|^2}{2\ell^2}\right), \tag{1}$$

with ℓ entering as a regression parameter.

If the energy is known at a set of parameter points $\bar{P}$ of size N $[\bar{E}(\bar{P}) = [E(\bar{p}_1), \ldots, E(\bar{p}_N)]^T$ with $\bar{p}_i \in \bar{P}]$, then the energy at some other point p can be estimated from the GP regression. As mentioned before, the combined set of energies $\bar{E}(\bar{P})$ and $E(p)$ is viewed as being sampled from a multivariate normal (or Gaussian) distribution with zero mean and covariance determined by the covariance function between points in the parameter space. This is expressed as

$$\begin{bmatrix} \bar{E}(\bar{P}) \\ E(p) \end{bmatrix} \sim \mathcal{N}\left(0, \begin{bmatrix} K(p, p) & K(p, \bar{P}) \\ K(\bar{P}, p) & K(\bar{P}, \bar{P}) \end{bmatrix}\right).$$

What we want then is the predicted value of $E(p)$ conditional on what is already known given the set of energies $\bar{E}(\bar{P})$. The probability distribution that predictions of $E(p)$ follows is given by the one-dimensional Gaussian distribution $\mathcal{N}(\mu, \sigma^2)$ with mean

$$\mu = K(p, \bar{P})K(\bar{P}, \bar{P})^{-1}\bar{E}(\bar{P}) \tag{2}$$

and variance

$$\sigma^2 = K(p, p) - K(p, \bar{P})K(\bar{P}, \bar{P})^{-1}K(\bar{P}, p). \tag{3}$$

The best predicted value for $E(p)$, which serves as the regression for the energy surface, is given by the mean

$$E(p) \approx \mu = K(p, \bar{P})K(\bar{P}, \bar{P})^{-1}\bar{E}(\bar{P}). \tag{4}$$

4. *Variational Monte Carlo calculations*

Energies at sample points in the K-NiO energy surface were obtained via VMC. For this study, VMC was applied as implemented within the QMCPACK package [37]. Single Slater-Jastrow [38,39] wave functions with one- and two-body Jastrow variational coefficients were used as the trial wave functions in the QMC algorithm. DFT single-particle orbitals for the QMC trial wave functions were generated by using QE and a plane-wave basis set with a 400 Ry energy cutoff and $4 \times 4 \times 4$ Monkhorst-Pack grids. The PBE + U exchange-correlation functional was used with the addition of Hubbard U of 4.7 eV on the Ni d orbital. DFT and VMC calculations for the GP study were performed by using scalar-relativistic norm-conserving pseudopotentials [40] which demonstrated accurate electronic properties for a bulk NiO in previous QMC studies [21,41]. To reduce the one-body finite-size effect in the supercell calculations, a twist-averaged boundary condition (TABC) [42] was employed by using a total of eight twists for the 64-atom cell.

5. *Gaussian process optimization of structure model via variational Monte Carlo*

The GP approach we use searches within a parametric domain that is assumed to contain the global energy minimum. As a conservative choice, we defined the parametric bounding domain to include displacements up to 4× greater

TABLE I. Optimized DFT K–O bond length for $K_{0.03}Ni_{0.97}O$ by various methods. The VMC total energy for each structure is also shown. For reference, the experimental Ni–O bond length for bulk NiO is 2.08 Å.

Method	K–O bond length (Å)	VMC energy (eV)
LDA	2.28	−157605.26(6)
LDA + U	2.28	−157606.49(8)
PBE	2.34	−157607.90(10)
PBE + U	2.36	−157608.26(8)
VMC + GP + quad	2.34	−157611.66(7)

than those observed in DFT for any of the parameters. If we denote the structure model as $S(p)$, then the energy surface we seek to minimize is $E(p) = E_{\mathrm{VMC}}(S(p))$. The energy surface was estimated via GP regression by building up energies sampled within the parametric domain to iteratively constrain the interpolated surface and its minimum. Sets of sample energies were generated via latin hypercube sampling (LHS) [43] of the parameters followed by VMC calculations performed on the sample structures. Latin hypercube sampling is an alternative to Monte Carlo sampling that has advantageous convergence properties for low-dimensional problems and no disadvantage relative to Monte Carlo sampling in higher dimensions.

The GP regression surface was built up iteratively in the following way. In each iteration a set of $(d + 2)(d + 1) + 1$ parameter samples was generated via LHS. For our four-dimensional structure parametrization, this corresponded to 31 samples in each round, which is double the number of samples sufficient to constrain a multidimensional quadratic function of dimension four. Variational Monte Carlo calculations were performed at each sampled structure and the energy surface was estimated via GP regression across the set of samples. The parametric search domain was then halved in each dimension around the minimum predicted via GP in each round. The process described above was then repeated in the reduced parameter domain. Following three rounds of GP optimization, the final optimal structure was estimated from the totality of sampled points using both Gaussian process and quadratic regressions. The final quadratic regression resulted in the lowest-energy structure overall (denoted "VMC + GP + quad" in Table I).

6. Geometry optimization of defect complexes using density functional theory

Starting with the optimized (K, Ni)O supercell geometry from the GP regression, as described above, we performed spin-polarized DFT + U calculations to investigate effects of the charge-state of K as well as other defect complexes on the atomic structure and bond lengths. These DFT calculations were performed by using the projector-augmented-wave method as implemented in the VASP package [44,45]. All calculations employed the PBE-GGA exchange-correlation functional [32], with a Hubbard $U = 4.7$ eV for the Ni d orbitals, using the rotationally invariant Dudarev method [35]. A 400 eV plane-wave energy cutoff was used with a $4 \times 4 \times 4$ Γ-centered k-point mesh for all the calculations. A conjugate-gradient method was used to relax the internal atomic coordinates of the structures at fixed lattice parameters of the supercell, until the energies were converged down to 1×10^{-4} eV between consecutive atomic relaxation steps.

A histogram analysis was performed on trajectories coming from *ab initio* molecular-dynamics (AIMD) simulations using VASP, accelerated at ∼1000 K using a Nose-Hoover thermostat. Simulations were run for ∼5 ps with a time step of 2 fs, and histograms have been plotted (Fig. 6) for the trajectories from the last ∼2.0 ps run.

D. Scanning transmission electron microscopy

The cross-section sample of the thin film was prepared along [1 0 0] by using the focused ion beam (FIB) method. The sample thickness was thinned down using varying ion current and successively lower energies starting at 30 kV and finishing at 2 kV. Atomic-resolution images of the thin film were acquired by using an aberration-corrected scanning transmission electron microscope (Themis Z, Thermo-Fisher Scientific) operated at 300 kV. The scanning transmission electron microscopy (STEM) images were acquired by using a high-angle annular dark-field (HAADF) detector with an inner collection angle of 46 mrad, a probe current of 30 pA, and a convergence semi-angle of 18 mrad. To reduce the image distortion due to the sample drift and scan noise, we recorded ten HAADF images from the same sample area using both 0° and 90° as the fast scan direction. The 0° scan direction is parallel to the substrate surface. The fast scan direction is free of the so-called fly back error, which is the largest source of noise in the acquired STEM images. A short dwell time of 1 μs was used for HAADF-STEM image acquisition. The images were first rotated and aligned by using a custom MATLAB script and averaged together. The averaged HAADF images of two different fast scan directions were used to calculate the lattice strain following the method in Ref. [46] for the strain parallel and perpendicular to the substrate surface, respectively.

III. RESULTS AND DISCUSSION

A. Calculation of the K–O bond distance in substitutionally doped NiO

The K–O bond lengths obtained from DFT and GP-VMC structural optimizations of the 64-atom supercell are shown in Table I along with the corresponding VMC total energies for each structure. As expected, the addition of U improves the DFT description of the electronic structure of K-NiO and of the resulting atomic structures, as judged by the VMC total energies of the DFT-relaxed structures. The lowest-energy structure was identified by VMC and GP regression by using the reduced structure model discussed in Sec. II C 2. By contrast, the DFT structural optimizations relaxed all atomic degrees of freedom simultaneously. Despite these differences, the DFT and VMC relaxed structures are in relatively near agreement about the nearest-neighbor K–O bond length, and the best overall theoretical prediction, via VMC and GP regression, yields a bond length of 2.34 Å.

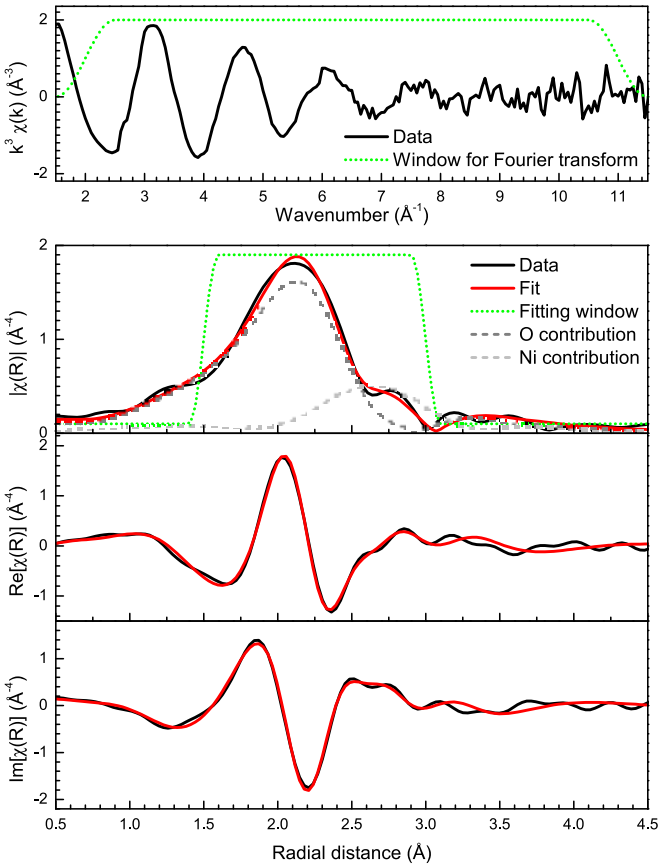

FIG. 4. Upper panel: k^3-weighted XAFS spectrum $k^3\chi(k)$ of (K, Ni)O on $NdScO_3$ at the potassium K edge. The black line denotes the data, and the dotted green line shows the window for the Fourier transform. Lower panel: Magnitude ($|\chi(R)|$), real ($\mathrm{Re}[\chi(R)]$), and imaginary part ($\mathrm{Im}[\chi(R)]$) of the Fourier transform of the k^3-weighted XAFS spectrum above. Black lines denote the data, red lines are the fit, and the green dotted line shows the fitting window. Dashed dark and light-gray lines denote the contribution of the K–O and K–Ni scattering paths to the radial distribution function.

B. X-ray absorption fine structure

1. Data acquisition and processing

The oscillatory part $\chi(E)$ of the measured absorption spectrum $\mu(E)$ was extracted by subtracting a background function $\mu_0(E)$ (as shown in the Supplemental Material [23]) and normalizing to the edge jump $\Delta\mu_0(E_0)$, which is calculated through extrapolation of preedge and postedge background to the absorption edge energy E_0:

$$\chi(E) = \frac{\mu(E) - \mu_0(E)}{\Delta\mu_0(E_0)}. \tag{5}$$

$\chi(E)$ was then converted to $\chi(k)$ with $k = [2m(E - E_0)/\hbar^2]^{1/2}$ where m is the electron mass.

We measured XAFS at the potassium K edge (Fig. 4) on a 42 nm (K,Ni)O thin film grown on $NdScO_3$ at a doping level of 3.9%, with a buffer layer of 12 nm NiO, and a capping layer of 2 nm NiO. The oscillations in $\chi(E)$ die off quickly, indicating high disorder.

A prominent feature in the potassium K-edge spectrum caused by multiple electron excitations (MEEs) [47] at $k = 9.6$ Å^{-1} was removed (for details see Supplemental Material [23]). Other MEEs were found not to influence the analysis significantly and were therefore left untouched.

TABLE II. Results of the fit to the EXAFS spectra shown in Fig. 4.

Variable	Value
S_0^2	Fixed to 0.93
ΔE_0	4.4 ± 0.4 eV
K–O distance	2.695 ± 0.009 Å
σ^2 (K–O)	0.0215 ± 0.0005 Å^2
K–Ni distance	3.03 ± 0.02 Å
σ^2 (K–Ni)	0.058 ± 0.003 Å^2

2. Fitting procedure

The fits were done on the Fourier transform of the k^3 weighted $\chi(k)$, $\chi(R)$, using the DEMETER package [48]. The Fourier transform was taken within a k range of 2–11 Å^{-1} and fitting was carried out between 1.5 and 3.0 Å. The FEFF 6.0 code [49] is implemented in DEMETER and calculates the contribution of all possible scattering events in a given input structure.

We fit the values for the amplitude factor S_0^2, ΔE_0, the distance between K and the first shell of O (K–O distance), the distance between K and the first shell of Ni (K–Ni distance), and the mean-square deviation from the mean length of these two distances σ^2(K–O), and σ^2(K–Ni). This adds up to six fitting parameters compared with only eight independent data points. To reduce the number of parameters, we restrained the amplitude factor S_0^2 for all fits discussed in this work. We tested different values for S_0^2 and within the range of reasonable values between 0.7 and 1.0, the remaining five parameters remained unchanged within the error bar. The fit with the lowest χ^2 was obtained for $S_0^2 = 0.93$, which is the value that was used for the remainder of the fits.

For the input structure of a first fit, we replaced one nickel atom at the center of a 64-atom rocksalt-type unit cell with potassium and relaxed the structure within a GGA + U calculation. The K–O bond length resulting from the GGA + U calculation was 2.34 Å and the result of the fit was 2.74 Å.

Because of the large deviation in K–O bond length from that of the input structure, we created a new one. We constrained the K–O bond length to 2.74 Å, equal to that resulting from the first fit, and relaxed the remaining atomic positions within GGA + U. We repeated the FEFF calculation and the fit, which resulted in a K–O bond length of 2.695 ± 0.008 Å. Data and fit are shown in Fig. 4 and the resulting values are summarized in Table II.

Although the discrepancy with theory—both DFT and QMC—is smaller than assumed after the first fit, with about 0.35 Å it is still high with a difference of 14% between theory and experiment. As a comparison, the Ni–O bond length increases only by 8% when comparing trivalent nickel in $LaNiO_3$ [50] to divalent nickel in NiO [51] and typical errors in DFT structure calculations are less than 0.1 Å [52]. In the following paragraphs we discuss possible explanations.

3. Impact of fitting parameters and ranges

First, we tested the robustness and validity of the fit by varying the range for the Fourier transform of the XAFS spectrum (see Supplemental Material [23]). We found that the resulting deviations are well below the error bars.

The raw XAFS spectrum $k^3\chi(k)$ clearly shows one dominant contribution, which corresponds to the strongest peak in the radial distribution function $|\chi(R)|$ and the K–O scattering path. The Fourier transform of the data reveals the presence of at least one additional contribution to the XAFS spectrum. It peaks at about 2.75 Å in $|\chi(R)|$ and corresponds to the K–Ni scattering path.

We tested the impact of the second scattering path by removing the nickel shell from the fit. To compare fits with different numbers of fitting parameters, we need to consider the reduced χ^2 (χ^2_{red}), which is χ^2 normalized to the degrees of freedom rather than χ^2 itself. The increase in χ^2_{red} from 11 to 53 indicates that K–Ni is indeed needed to properly describe the spectrum. The reduction of χ^2_{red} to 37 upon reducing the fitting range of $|\chi(R)|$ to 1.5–2.6 Å, which mainly contains the contribution from K–O, confirms the existence of a K–Ni scattering path and therefore that K is dissolved in the NiO matrix. This finding disproves an alternative explanation of the discrepancy between experiment and theory; namely, that K is not solved in the NiO matrix but either floats on top of the sample or forms clusters within the film.

The measured K–Ni distance is 0.08 Å longer than the Ni–Ni distance in undoped NiO and 0.06 Å and 0.10 Å longer than predicted by PBE + U and by VMC, respectively. This is just within the limit of a typical DFT accuracy. It is surprising, though, that VMC, which should be more accurate than DFT, results in a seemingly worse agreement with experiment.

4. Discussion of the mean-square variation of bond lengths

The resulting mean square variations σ^2 of both, K–O and K–Ni, are large. Typical values for σ^2 in single crystals are on the order of 10^{-3} Å^2. Here, σ^2 is an order of magnitude higher; i.e., 0.02 and 0.06 Å^2 for the K–O and the K–Ni scattering path, respectively. In fact, σ^2 (K–O) is comparable to σ^2 (K–O) in an aqueous solution of K^+ [47] and in K_2O-B_2O_3 glasses [53] which indicates high disorder. For such high values, the assumption of a Gaussian model, meaning it is just as likely to find a bond distance that is by an amount a shorter than the average bond distance as it is to find a bond distance that is by an amount a longer, is no longer valid.

To obtain an accurate result for the bond length, it would be necessary to include anharmonic effects [54]. However, these effects mainly contribute to the high-k region of the spectrum where the signal-to-noise ratio of our data is very low. Due to the low amount of dopant in our samples (a small fraction of a very thin film) and due to the high disorder, it is extremely difficult to obtain high-quality data in the high-k region of the spectrum. In fact, the data acquisition would take so long that it is unfeasible. Therefore, we did not include anharmonic effects in our analysis.

This omission can make measured bond distances appear shorter than they actually are. Given the similarity of

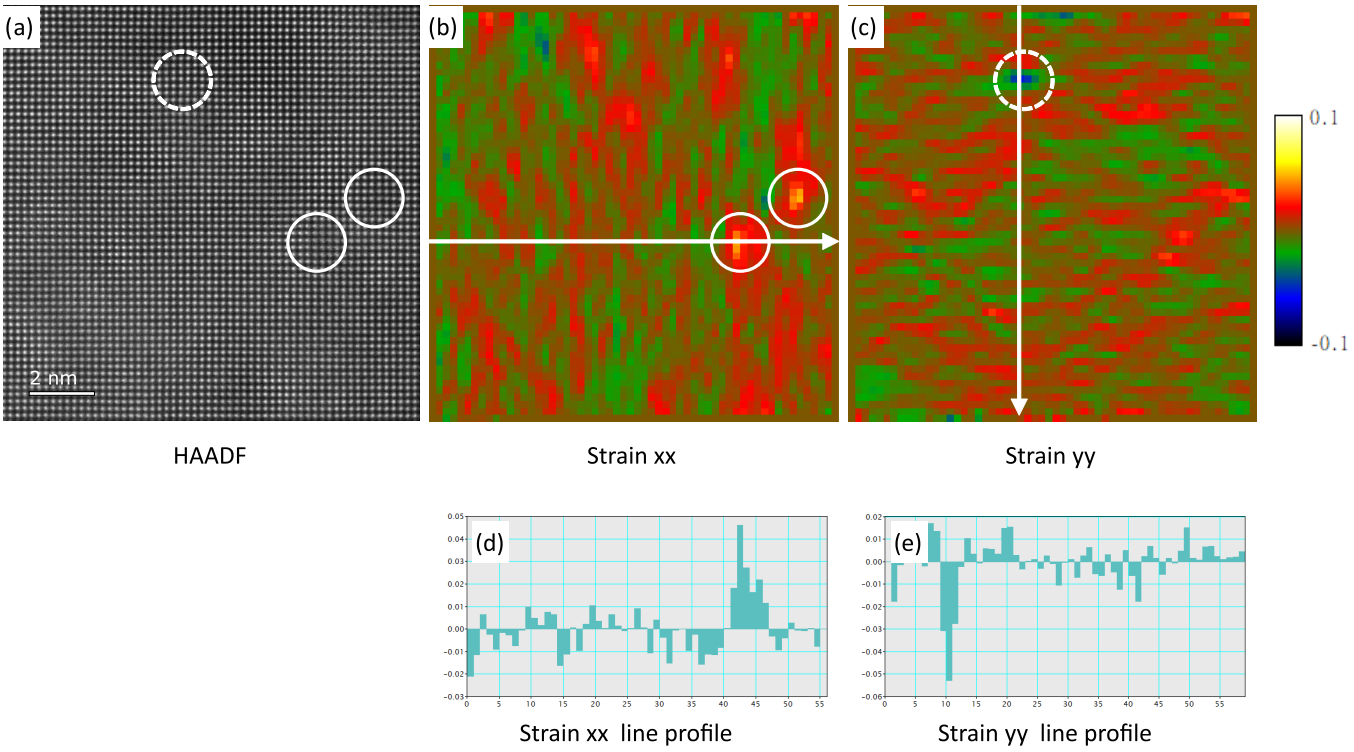

FIG. 5. TEM images of a NiO thin film doped with 3.6% potassium. (a) High-angle annular dark field image. The white circles mark regions of high tensile and compressive strain as identified through the strain maps in panels (b) and (c). (b) Strain map along the x direction (parallel to the substrate surface). (c) Strain map along the y direction (parallel to growth direction). (d) Line profile of the strain in the x direction shown for the line in panel (b). (e) Line profile of the strain in the y direction shown for the line in panel (c).

our XAFS to Ref. [47], where anharmonic effects were included in the fit, we estimate that the true K–O bond length is at most ∼0.05 Å longer than the one obtained from the fit (Table II) and we can conclude that anharmonic effects cannot explain the discrepancy between theory and experiment.

5. Discussion of coordination number

In principle, XAFS allows us to determine the number of atoms in a shell around the central absorbing atom; i.e., the coordination number N. If, however, σ^2 is as large as in the present case, a determination of N cannot be exact because σ^2 and the coordination number are highly correlated. To get an estimate for the uncertainty, we changed the coordination number of oxygen and nickel around the potassium dopant in separate fits (see Supplemental Material [23]). The change of coordination number does not have a significant impact on the fit for nickel. With keeping the amplitude factor S_0^2 between its reasonable values 0.7 and 1.0, we obtained reasonable fits when N is between 5 and 9 for oxygen. Therefore, we suspect that the formation of oxygen and/or nickel vacancies around potassium is responsible for the high disorder and for the discrepancy with theory, which we discuss later.

C. Comparison with transmission electron microscopy

To complement XAFS and find further support for potassium being incorporated into our NiO thin films, we studied STEM images. A direct probe of potassium via STEM coupled with electron energy-loss spectroscopy (EELS) was not feasible due to the low dopant concentration and an overlap of the potassium with the carbon edge. Instead, we looked at strain maps. We measured the position of each atom and calculated the deviation of the position of each atom from a reference lattice (assumed to be a perfect lattice), which gives the displacement from the reference lattice for individual atoms and the local strain. Color maps of the local strain parallel to the substrate/film interface or the x direction (growth direction or y direction) are shown in Figs. 5(b) and 5(c). Red, yellow, and white correspond to tensile strain and blue and green correspond to compressive strain. We found several spots with high tensile strain in the x direction (marked by white solid circles) and with high compressive strain in the y direction (marked by white dashed circles). The noise levels of the strain measurements along the xx and yy directions are ±0.0093 and ±0.0085, respectively, which is consistent with a previous measurement performed on a STO substrate [46]. The large local strains in the maps are approximately four to five times higher than the noise. We suggest that these local distortions are related to potassium incorporation.

D. Calculation of the K–O bond distance in defect complexes

For the (K,Ni)O system, the relaxed K–O (2.30 Å), K–Ni (2.96 Å), and Ni–O (2.11 Å) bond-lengths were similar to the PBE + U results obtained from QE. Changing the charge-state of the K atoms to $q = -1$, to simulate a "hole" in the valence band did not seem to appreciably change these bond lengths. Next, we decided to look at complexes with nickel vacancies (K-Ni$_v$) and oxygen vacancies (K-O$_v$), where the vacancies were created at sites closest to the K defect. Removing a Ni atom led to a slight increase in the nearest-neighbor K–Ni distance, but left the other bond distances relatively unchanged. But creating an oxygen vacancy gave rise to a significant spread in the nearest-neighbor K–O bond distances, from 2.29 to 2.48 Å, increasing the spread on the possible K–O bond lengths in our model.

Inspired by this observation, we further decided to look at the neutral K-O$_v$-K cluster. Such neutral-defect clusters have been observed in other cubic oxides [55] and as such could form even in NiO. Two configurations for the K-O$_v$-K clusters were generated—one where the three defects formed a chain (config1), and another where the K defects were on near-neighbor sites, and their closest oxygen-atom was removed (config2). Energetically, these two configurations were close to each other, differing by ∼5 meV/atom but the bond lengths showed significant differences and spread from the ideal (K, Ni)O geometry. Indeed, the largest K–O

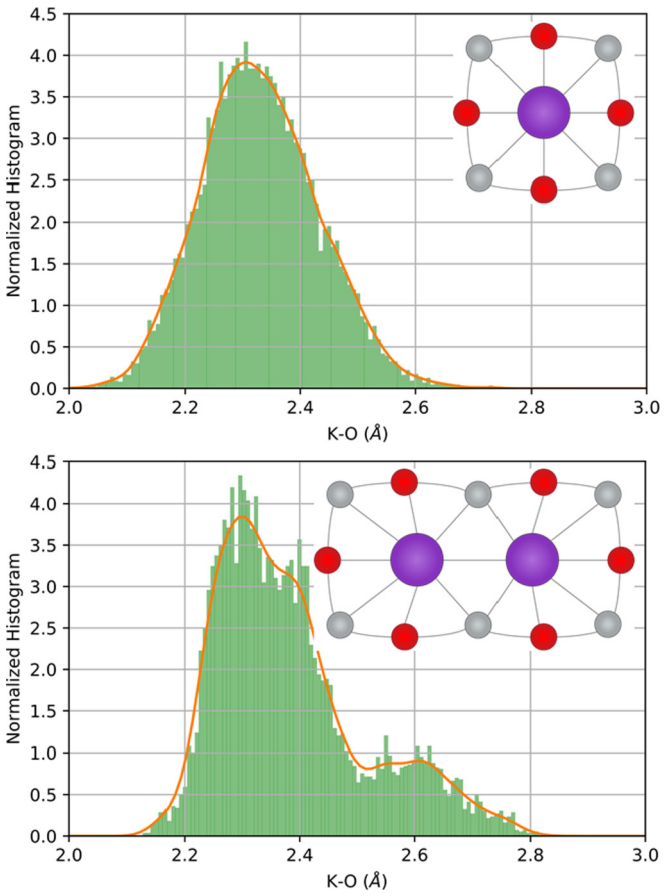

FIG. 6. Histogram (normalized to integrate to 1) plots of K–O nearest-neighbor distances for the single "K" substitutionally doping a "Ni" site (upper panel) and a K-O$_v$-K defect (lower panel) in a NiO supercell. Insets, where purple spheres correspond to K, gray spheres to Ni, and red spheres to oxygen, show a simplified structure and are not drawn to scale. The histograms were collected from trajectories collected from *ab initio* molecular-dynamics simulations at 1000 K, as explained in Sec. III D.

nearest-neighbor distance (config1) was 2.52 Å, much closer to the experimental observation. Given that our calculations were at 0 K, while the experiments were performed at room temperature, we suspect that the presence of such K-O_v-K clusters in the material can lead to an even larger K–O distance than what is seen in our models and could explain the unexpectedly large K–O distance measured in our XAFS experiments. To validate this assumption, we performed a histogram analysis for substitutionally doped NiO (Fig. 6, upper panel) and compared it with a histogram analysis of config1 (Fig. 6, lower panel) from an *ab initio* molecular-dynamics simulation. Indeed, the latter shows two maxima, one of them located at ∼2.6 Å, which is very close to the experimentally measured value. Therefore, we conclude that the large K–O bond distance seen in experiments can be rationalized by the presence of different defect complexes involving oxygen vacancies that are presumably disordered throughout the sample.

IV. SUMMARY AND CONCLUSION

In the presented work we have studied potassium-doped NiO thin films in order to demonstrate that potassium can, in spite of its large size, be incorporated in NiO thin film. This opens an important avenue for hole doping NiO, which is of interest from the point of view of applications. While NiO can be hole doped by using Li, the different deposition conditions for potassium doping compared with Li doping opens up a broader processing window. Our XAFS structural analysis indicates that the K–O bond length is 2.695 Å or slightly larger, while the theoretical results from DFT and VMC suggest a K–O bond length of 2.28 to 2.36 Å. One potential explanation for this discrepancy is that potassium is not fully dissolved in the nickel oxide matrix and instead forms clusters or floats to the surface. However, we did find a K–Ni scattering path in the XAFS analysis which proves that potassium is at least embedded in a NiO matrix.

The high values for σ^2 in the fits to the XAFS spectrum indicate a relatively large degree of disorder, which is a possible explanation for the discrepancy between experiment and theory. We found that the result of the fit is insensitive to the number of next-nearest nickel and that any value between 5 and 9 for the number of next-nearest oxygen gives reasonable results. We therefore suspected that oxygen and/or nickel vacancies are formed in the vicinity of potassium because of its size. This was supported by DFT and *ab initio* molecular-dynamics simulations. In particular, a configuration of K–(O-vacancy)–K resulted in one of the remaining five K–O bond distances to be close to the experimentally measured value. This leads to our conclusion that a combination of oxygen vacancy formation and disorder leads to the apparent discrepancy between experiment and theory, despite the nominally low K concentration.

Despite the above-mentioned pitfalls of introducing a dopant as large as potassium into nickel oxide, our work shows that potassium is fully incorporated into the nickel oxide matrix as a hole dopant. In a separate forthcoming work we will focus on the electronic structure of potassium-doped NiO. In spite of the presence of defect structures, such as K–(O-vacancy)–K defect structure, we will show that potassium systematically changes the band gap and introduces new states close to the Fermi level without closing the gap and without inducing a metallic state.

ACKNOWLEDGMENTS

The authors thank Mahalingam Balasubramanian for fruitful discussions and guidance in the XAFS analysis.

This research used resources of the Advanced Photon Source, a US Department of Energy (DOE) Office of Science User Facility operated for the DOE Office of Science by Argonne National Laboratory under Contract No. DE-AC02-06CH11357. F.W, H.S, P.G., A.B., P.R.C.K., O.H., and A.B. were supported by the US Department of Energy, Office of Science, Basic Energy Sciences, Materials Sciences and Engineering Division, as part of the Computational Materials Sciences Program and Center for Predictive Simulation of Functional Materials. An award of computer time was provided by the Innovative and Novel Computational Impact on Theory and Experiment (INCITE) program. This research used resources of the Argonne Leadership Computing Facility, which is a DOE Office of Science User Facility supported under Contract No. DE-AC02-06CH11357. VASP-DFT-based calculations used resources of the National Energy Research Scientific Computing Center (NERSC), a US Department of Energy Office of Science User Facility operated under Contract No. DE-AC02-05CH11231. Use of the Center for Nanoscale Materials, an Office of Science user facility, was supported by the US Department of Energy, Office of Science, Office of Basic Energy Sciences, under Contract No. DE-AC02-06CH11357.

This paper has been authored by UT-Battelle, LLC under Contract No. DE-AC05-00OR22725 with the US Department of Energy. The United States Government retains and the publisher, by accepting the article for publication, acknowledges that the United States Government retains a nonexclusive, paid-up, irrevocable, worldwide license to publish or reproduce the published form of this paper, or allow others to do so, for United States Government purposes. The Department of Energy will provide public access to these results of federally sponsored research in accordance with the DOE Public Access Plan [56].

[1] J. G. Bednorz and K. A. Müller, Z. Phys. B: Condens. Matter **64**, 189 (1986).

[2] H. Thomas, A. Marian, A. Chervyakov, S. Stückrad, D. Salmieri, and C. Rubbia, Renewable Sustainable Energy Rev. **55**, 59 (2016).

[3] Z. Wang, P. K. Nayak, J. A. Caraveo-Frescas, and H. N. Alshareef, Adv. Mater. **28**, 3831 (2016).

[4] F. Medina, P. Salagre, J. Sueiras, and J. Fierro, J. Mol. Catal. **81**, 387 (1993).

[5] F. Medina, P. Salagre, J. G. Fierro, and J. Sueiras, J. Catal. **142**, 392 (1993).

[6] P. K. Jana, S. Sarkar, and B. Chaudhuri, J. Phys. D: Appl. Phys. **40**, 556 (2007).

[7] H. Takagi and H. Y. Hwang, Science **327**, 1601 (2010).

[8] G. A. Sawatzky and J. W. Allen, Phys. Rev. Lett. **53**, 2339 (1984).

[9] F. L. A. Machado, P. R. T. Ribeiro, J. Holanda, R. L. Rodríguez-Suárez, A. Azevedo, and S. M. Rezende, Phys. Rev. B **95**, 104418 (2017).

[10] D. Alders, L. H. Tjeng, F. C. Voogt, T. Hibma, G. A. Sawatzky, C. T. Chen, J. Vogel, M. Sacchi, and S. Iacobucci, Phys. Rev. B **57**, 11623 (1998).

[11] P. T. Barton, Y. D. Premchand, P. A. Chater, R. Seshadri, and M. J. Rosseinsky, Chem. - Eur. J. **19**, 14521 (2013).

[12] V. Bianchi, D. Caurant, N. Baffier, C. Belhomme, E. Chappel, G. Chouteau, S. Bach, J. Pereira-Ramos, A. Sulpice, and P. Wilmann, Solid State Ionics **140**, 1 (2001).

[13] P. Kuiper, G. Kruizinga, J. Ghijsen, G. A. Sawatzky, and H. Verweij, Phys. Rev. Lett. **62**, 221 (1989).

[14] L. K. Wagner, J. Phys.: Condens. Matter **19**, 343201 (2007).

[15] P. Hohenberg and W. Kohn, Phys. Rev. **136**, B864 (1964).

[16] W. Kohn and L. Sham, Phys. Rev. **140**, A1133 (1965).

[17] A. Maachou, B. Amrani, and M. Driz, Phys. B (Amsterdam, Neth.) **388**, 384 (2007).

[18] L. Mitas, Curr. Opin. Solid State Mater. Sci. **2**, 696 (1997).

[19] D. Cremer, Wiley Interdiscip. Rev. Comput. Mol. Sci. **3**, 482 (2013).

[20] R. D. Shannon, Acta Crystallogr., Sect. A: Cryst. Phys., Diffr., Theor. Gen. Crystallogr. **32**, 751 (1976).

[21] H. Shin, Y. Luo, P. Ganesh, J. Balachandran, J. T. Krogel, P. R. C. Kent, A. Benali, and O. Heinonen, Phys. Rev. Mater. **1**, 073603 (2017).

[22] M. Yang, H. Pu, Q. Zhou, and Q. Zhang, Thin Solid Films **520**, 5884 (2012).

[23] See Supplemental Material at http://link.aps.org/supplemental/10.1103/PhysRevMaterials.3.115003 for detailed information on XAFS data processing and fits and x-ray diffraction.

[24] M. Mayer, *SIMNRA Users Guide* (Max-Planck-Institut fuer Plasmaphysik, Garching, Germany, 1997).

[25] W. McMillan, Phys. Rev. **138**, A442 (1965).

[26] R. Archibald, J. T. Krogel, and P. R. C. Kent, J. Chem. Phys. **149**, 164116 (2018).

[27] A. O'Hagan and J. F. C. Kingman, J. Roy. Stat. Soc. B Met. **40**, 1 (1978).

[28] P. Giannozzi, S. Baroni, N. Bonini, M. Calandra, R. Car, C. Cavazzoni, D. Ceresoli, G. L. Chiarotti, M. Cococcioni, I. Dabo, A. D. Corso, S. de Gironcoli, S. Fabris, G. Fratesi, R. Gebauer, U. Gerstmann, C. Gougoussis, A. Kokalj, M. Lazzeri, L. Martin-Samos, N. Marzari, F. Mauri, R. Mazzarello, S. Paolini, A. Pasquarello, L. Paulatto, C. Sbraccia, S. Scandolo, G. Sclauzero, A. P. Seitsonen, A. Smogunov, P. Umari, and R. M. Wentzcovitch, J. Phys.: Condens. Matter **21**, 395502 (2009).

[29] E. I. Alessandrini and J. F. Freedman, Acta Crystallogr. **16**, 54 (1963).

[30] D. M. Ceperley and B. J. Alder, Phys. Rev. Lett. **45**, 566 (1980).

[31] J. P. Perdew and A. Zunger, Phys. Rev. B **23**, 5048 (1981).

[32] J. P. Perdew, K. Burke, and M. Ernzerhof, Phys. Rev. Lett. **77**, 3865 (1996).

[33] J. P. Perdew, K. Burke, and M. Ernzerhof, Phys. Rev. Lett. **78**, 1396 (1997).

[34] V. I. Anisimov, J. Zaanen, and O. K. Andersen, Phys. Rev. B **44**, 943 (1991).

[35] S. L. Dudarev, G. A. Botton, S. Y. Savrasov, C. J. Humphreys, and A. P. Sutton, Phys. Rev. B **57**, 1505 (1998).

[36] R. Grimm and R. Storer, J. Comput. Phys. **7**, 134 (1971).

[37] J. Kim, A. D. Baczewski, T. D. Beaudet, A. Benali, M. C. Bennett, M. A. Berrill, N. S. Blunt, E. J. L. Borda, M. Casula, D. M. Ceperley, S. Chiesa, B. K. Clark, R. C. Clay, K. T. Delaney, M. Dewing, K. P. Esler, H. Hao, O. Heinonen, P. R. C. Kent, J. T. Krogel, I. Kylänpää, Y. W. Li, M. G. Lopez, Y. Luo, F. D. Malone, R. M. Martin, A. Mathuriya, J. McMinis, C. A. Melton, L. Mitas, M. A. Morales, E. Neuscamman, W. D. Parker, S. D. P. Flores, N. A. Romero, B. M. Rubenstein, J. A. R. Shea, H. Shin, L. Shulenburger, A. F. Tillack, J. P. Townsend, N. M. Tubman, B. V. D. Goetz, J. E. Vincent, D. C. Yang, Y. Yang, S. Zhang, and L. Zhao, J. Phys.: Condens. Matter **30**, 195901 (2018).

[38] J. C. Slater, Phys. Rev. **34**, 1293 (1929).

[39] R. Jastrow, Phys. Rev. **98**, 1479 (1955).

[40] J. T. Krogel, J. A. Santana, and F. A. Reboredo, Phys. Rev. B **93**, 075143 (2016).

[41] C. Mitra, J. T. Krogel, J. A. Santana, and F. A. Reboredo, J. Chem. Phys. **143**, 164710 (2015).

[42] C. Lin, F. H. Zong, and D. M. Ceperley, Phys. Rev. E **64**, 016702 (2001).

[43] M. D. McKay, R. J. Beckman, and W. J. Conover, Technometrics **21**, 239 (1979).

[44] P. E. Blöchl, Phys. Rev. B **50**, 17953 (1994).

[45] G. Kresse and D. Joubert, Phys. Rev. B **59**, 1758 (1999).

[46] J.-M. Zuo, A. B. Shah, H. Kim, Y. Meng, W. Gao, and J.-L. Rouviére, Ultramicroscopy **136**, 50 (2014).

[47] V.-A. Glezakou, Y. Chen, J. L. Fulton, G. K. Schenter, and L. X. Dang, Theor. Chem. Acta **115**, 86 (2006).

[48] B. Ravel and M. Newville, J. Synchrotron Radiat. **12**, 537 (2005).

[49] S. I. Zabinsky, J. J. Rehr, A. Ankudinov, R. C. Albers, and M. J. Eller, Phys. Rev. B **52**, 2995 (1995).

[50] J. Yang, Acta Crystallogr., Sect. B: Struct. Sci. **64**, 281 (2008).

[51] S. Sasaki, K. Fujino, and Y. Takeuchi, Proc. Jpn. Acad., Ser. B **55**, 43 (1979).

[52] J. Heyd and G. E. Scuseria, J. Chem. Phys. **121**, 1187 (2004).

[53] Y. Kita, N. Umesaki, K. Handa, T. Fukunaga, M. Misawa, and T. Iida, Proc. – Electrochem. Soc. **1998-11**, 574 (1998).

[54] E. Daryl Crozier, Phys. B (Amsterdam, Neth.) **208-209**, 330 (1995).

[55] J. Ding, J. Balachandran, X. Sang, W. Guo, J. S. Anchell, G. M. Veith, C. A. Bridges, Y. Cheng, C. M. Rouleau, J. D. Poplawsky, N. Bassiri-Gharb, R. R. Unocic, and P. Ganesh, Chem. Mater. **30**, 4919 (2018).

[56] https://www.energy.gov/downloads/doe-public-access-plan.